OPEN ACCESS
IOP Publishing
Plasma Sources Science and Technology
Plasma Sources Sci. Technol. **34** (2025) 045017 (15pp)
https://doi.org/10.1088/1361-6595/adcb6b

Experimental and numerical study of the ionization-attachment instability in an O_2 capacitively coupled radio frequency plasma

Ranna Masheyeva[1,2,3,*], Mate Vass[1,4], Murat Myrzaly[2], Chong-Biao Tian[4,5], Karlygash Dzhumagulova[2,3], Julian Schulze[4], Zoltán Donkó[1] and Peter Hartmann[1]

[1] Institute for Solid State Physics and Optics, HUN-REN Wigner Research Centre for Physics, 1121 Budapest, Hungary
[2] Research Institute of Experimental and Theoretical Physics, Al-Farabi Kazakh National University, Almaty 050040, Kazakhstan
[3] Satbayev University, Almaty 050000, Kazakhstan
[4] Chair of Applied Electrodynamics and Plasma Technology, Faculty of Electrical Engineering and Information Sciences, Ruhr University Bochum, 44801 Bochum, Germany
[5] Key Laboratory of Materials Modification by Laser, Ion, and Electron Beams (Ministry of Education), School of Physics, Dalian University of Technology, Dalian 116024, People's Republic of China

E-mail: masheyeva.ranna@gmail.com

Received 12 December 2024, revised 24 March 2025
Accepted for publication 10 April 2025
Published 23 April 2025

Abstract

This study examines the emergence of an ionization-attachment plasma instability in a geometrically symmetric capacitively coupled plasma reactor with stainless steel electrodes operated in oxygen. Periodic fluctuations in optical emission intensity were observed under varying conditions of pressure and voltage. To interpret the experimental data, a kinetic (PIC/MCC) simulation approach was employed, with a particular focus on the influence of external parameters, including the voltage amplitude and the O_2^+ ion induced secondary electron emission coefficient (SEEC, γ). By varying the γ coefficient at fixed pressure and voltage amplitude, the aim was to achieve the best possible agreement between the measured and computed oscillation frequencies. The experimentally observed oscillation frequency of $f_{\mathrm{in}} = 0.25$ kHz at $\phi_0 = 655$ V voltage amplitude (with 13.56 MHz RF excitation) was reproduced in the simulation with $\gamma = 0.0042$ at $\phi_0 = 600$ V. The results highlight the critical role of these parameters in the onset and characteristics of plasma instability and correspond to a computationally assisted diagnostic to determine ion induced secondary electron emission coefficients.

* Author to whom any correspondence should be addressed.

Original Content from this work may be used under the terms of the Creative Commons Attribution 4.0 licence. Any further distribution of this work must maintain attribution to the author(s) and the title of the work, journal citation and DOI.

© 2025 The Author(s). Published by IOP Publishing Ltd

Keywords: capacitively coupled plasma, particle in cell simulation, instability

1. Introduction

Low temperature capacitively coupled plasmas (CCPs) are commonly used in various industrial applications including microelectronics and biomedical applications [1, 2]. In particular, electronegative gases, including Cl_2, CF_4, SF_6 and O_2 are utilized in industrial processes such as plasma etching, semiconductor manufacturing, and gas insulation [3–5]. The presence of negative ions in a discharge has a marked effect on the plasma dynamics, giving rise to a variety of instabilities associated with the electronegativity of the gas [2, 3, 6–8]. A comprehensive understanding of, and ability to control, plasma instabilities in electronegative gases is essential for optimizing a wide range of industrial and scientific applications.

Descoeudres *et al* [7] observed an attachment-induced ionization instability experimentally in O_2 and CF_4 capacitive RF discharges using time-resolved voltage probe, Langmuir probe, optical emission, and mass spectrometry measurements. At a gas pressure of 25 Pa, the instability was observed to occur for peak-to-peak voltages (V_{pp}) between 185 and 480 V in O_2 discharges, and between 220 and 550 V in CF_4 discharges with the frequency of the oscillations in the kilohertz range. The frequency of the oscillations was observed to be approximately 3.5 kHz in O_2 and around 80 kHz in CF_4. It was found that the plasma remained stable below 19.5 Pa in O_2 and 10 Pa in CF_4 at $V_{pp} = 250$ V.

The results of the Descoeudres *et al* [7] for oxygen are in alignment with those of Katsch *et al* [9], wherein the unstable zone was identified at approximately 30 Pa and 300 V in a capacitively coupled 13.56 MHz radio frequency (RF) oxygen discharge in the Gaseous Electronics Conference Reference Cell. Furthermore, Descoeudres *et al* observed that the SF_6 plasma is stable under all of their experimental conditions [7]. The observations have been explained by considering the attachment and ionization cross sections of these gases and by applying the theoretical instability criterion of Nighan and Wiegand [8], which showed that O_2 and CF_4 plasmas are unstable at low electron temperature, and that the SF_6 plasma is stable due to its particular low-energy attachment cross section. As in the case of [7], oscillations in the kilohertz (from 0.3 to 3 kHz) range were observed experimentally by Küllig *et al* [10] in capacitively coupled RF (13.56 MHz) oxygen plasma. In these systems, the electron attachment and detachment processes have been identified as the primary sources of instability. Additionally, electron heating and metastable molecules in electronegative discharges have been found to play a role in the observed instabilities. Furthermore, microsecond-scale instability phenomena were observed in a capacitive CF_4/Ar (1:9) plasma driven at 13.56 MHz at a pressure of 150 mTorr ($\approx$ 20 Pa) in [11] using a one-dimensional fluid/Monte Carlo (MC) hybrid model. Fluctuations were found in the densities and fluxes of charged particles, the electric field, as well as the rates of electron impact reactions, particularly in the bulk. The effects of changes in the gap distance and driving power on the fluctuation amplitudes and instability period were also investigated. The study noted that in the mixture discharge, the ionization of Ar metastables and the dissociative attachment of CF_4 played a minor role, in contrast to the predominant influence of Ar ionization and excitation.

Although the focus of our study is on CCPs, inductively coupled plasmas also exhibit instabilities, but for different reasons. For instance, Lieberman *et al* [12] observed plasma instabilities, i.e. a temporal modulation of the optical emission and of the charged particle densities at frequencies in the 1–900 kHz range in an O_2 and Ar/SF_6 mixture using a planar coil configuration. For describing these instabilities a global model was used, which was later improved by Chabert *et al* [13] for SF_6 and Ar/SF_6 mixtures. Similarly, Tuszewski and White [14] reported instabilities in O_2 and Ar/SF_6 discharges created in a cylindrical inductively coupled configuration driven at 0.46 MHz. They observed self-excited modulations in the ion current using a cylindrical Langmuir probe with frequencies in the range of 1–40 kHz [14]. Reproducible instabilities were observed in a low-pressure, 13.56 MHz inductively coupled gaseous electronics conference RF cell operating in oxygen [15]. In all these studies the instabilities were related to the transitions between inductive and capacitive modes leading to modulations of charged particle densities, electron temperature, and plasma potential.

Furthermore, the presence of dust particles was observed to induce instabilities, as documented in [16]. The underlying mechanism of this phenomenon also linked to the attachment-induced ionization instability, which has been previously observed in electronegative plasmas [7, 8]. This suggests that dust particles may act as a substitute for negative ions in these systems.

The underlying physical processes of the ionization-attachment instability formation are based on an initial increase in electron density, n_e, during natural fluctuations. In general, this increase results in a reduction in the electron temperature, T_e, due to an increase of the plasma conductivity and a decrease of the electric field required to drive the current through the plasma. The impact of this reduction in temperature varies depending on the specific characteristics of the gas in question. Generally, in electropositive gases where attachment processes are absent, the primary sources of electrons and ions are electron impact ionization, while the primary loss mechanisms are only diffusion to the walls and recombination. A reduction in electron temperature results in a decrease in ionization, which subsequently leads to a decline in electron density. Consequently, the initial increase in electron density is met with a subsequent decrease, resulting in a balanced fluctuation and the prevention of instability through

the establishment of a negative feedback loop. In contrast, in electronegative gases, electrons are additionally lost due to attachment, and the efficiency of this process is dependent upon the electron temperature. A reduction in electron temperature, accompanied by a lesser decline in attachment than ionization, results in a decrease in electron density. This is analogous to the stabilization of a perturbation observed in an electropositive gas. However, a reduction in electron temperature will result in an effective increase in electron density, if the attachment rate declines more rapidly than the ionization rate. This generates a positive feedback loop, leading to instability. In this type of instability, the primary sources of these oscillations are n_e and T_e, which in turn give rise to fluctuations of other plasma parameters.

This study examines the development of plasma instability through the investigation of periodic fluctuations in emitted light intensity in a CCP reactor. The reactor is geometrically symmetric and operated in oxygen gas under varying conditions of pressure and voltage. Furthermore, a 1d3v electrostatic particle-in-cell with Monte Carlo collisions (PIC/MCC) simulation approach is employed to interpret the experimental data and to elucidate the impact of system parameters, including the voltage amplitude and the O_2^+ ion induced secondary electron emission coefficient (SEEC, γ), on the emergence of the plasma instability. To achieve optimal agreement between the observed and calculated oscillation frequencies, the γ coefficient is adjusted while maintaining fixed pressure and voltage amplitude. The characteristics of oxygen CCPs depend on several surface coefficients such as the quenching coefficient of oxygen metastable molecules, the secondary electron emission yield, as well as the reflection coefficient of the electrons at the electrodes. As values for the quenching coefficient and the electron reflection became relatively well established for stainless steel surfaces [17, 18], we handle the (ion-induced) secondary electron yield in our work as an unknown quantity, more precisely as a fitting parameter. In this way γ can be determined and the proposed method corresponds to a computationally assisted diagnostic to measure such surface coefficients.

The paper is structured as follows: section 2 outlines the investigative methods, including the experimental setup and the simulation method. Section 3 presents and discusses the results of the measurements and simulations. Finally, section 4 offers a conclusion to this study.

2. Methods

2.1. Experimental setup

In the course of our investigation, we employ the geometrically symmetric Budapest v.3 plasma reactor [19]. A schematic representation of the experimental setup is provided in figure 1. The flat disk electrodes, composed of 304-grade stainless steel with identical diameters of $d = 140$ mm, are positioned within a quartz cylinder at a distance of 25 mm. No active cooling is applied to the electrodes. The chamber is evacuated via a turbomolecular and a rotary pump, resulting in a base pressure of approximately 10^{-5} Pa. The experiments are conducted with O_2 gas of 4.5 purity, delivered at a steady flow rate of approximately 1.5 sccm, regulated by a mass flow controller. A needle valve in the pump line enables precise control of the gas pressure within the chamber. The pressure is monitored by capacitive gauges (Pfeiffer Vacuum CMR264 and MKS Baratron 631A).

The upper electrode is driven by an RF power generator (Tokyo Hi-Power RF-150, 13.56 MHz generator), via an impedance matching box (MB-300). The lower electrode is grounded. The voltage drop across the discharge is monitored by a high voltage probe (Agilent 10 076A) connected to an oscilloscope (Hewlett Packard 54 602B).

The monitoring of light intensity emitted from the central region of the discharge is conducted using a ThorLabs APD130A2/M avalanche photodetector (50 MHz bandwidth, 200–1000 nm spectral sensitivity) and a PicoScope 6403B USB oscilloscope (350 MHz bandwidth). The PicoScope is linked to a computer for data acquisition, storage, and analysis. Furthermore, a charge-coupled device (CCD) camera (Allied Vision Prosilica GX1050) equipped with a bi-telecentric lens (ThorLabs MVTC23005) is utilized for the capture of the axial distribution of the emitted light intensity. For the above both optical diagnostics no optical filters are used, i.e. wavelength integrated measurements are performed.

The experiments are conducted at a fixed driving frequency of 13.56 MHz, at pressures between 50 Pa and 350 Pa, and voltage amplitudes, ϕ_0, between 250 V and 700 V.

2.2. Computational method

The numerical results are obtained from a 1d3v PIC/MCC code, which has been introduced in detail in [20]. The species traced in the simulations are e^-, O_2^+ ions, and O^- ions. The model includes 23 elementary collision processes, which are listed in table 1.

Collisions between electrons and O_2 molecules include elastic scattering, rotational and vibrational excitation, metastable excitation, dissociative attachment, electronic excitation, dissociation, ionization, and dissociative excitation as well as electron impact detachment of O^- ions and dissociative recombination of O_2^+ ions are also taken into account. The $e^- + O_2$ process list and cross sections adopted are largely based on the 'xpdp1' set [22]. More details of the model can be found in [20].

The O_2^+ ions can collide with the background gas molecules elastically, resulting in either isotropic scattering or charge exchange. The cross sections for these processes are taken from Gudmundsson's work [23]. In case of the $O^- + O_2$ collisions elastic scattering and detachment are considered [23]. Mutual neutralization of O^- and O_2^+ ions and associative detachment between O^- ions and $O_2(a^1\Delta_g)$ singlet delta oxygen molecules are also included in the model. The metastable molecules are not traced in the simulation, however, their density is calculated based on a diffusion balance equation (see

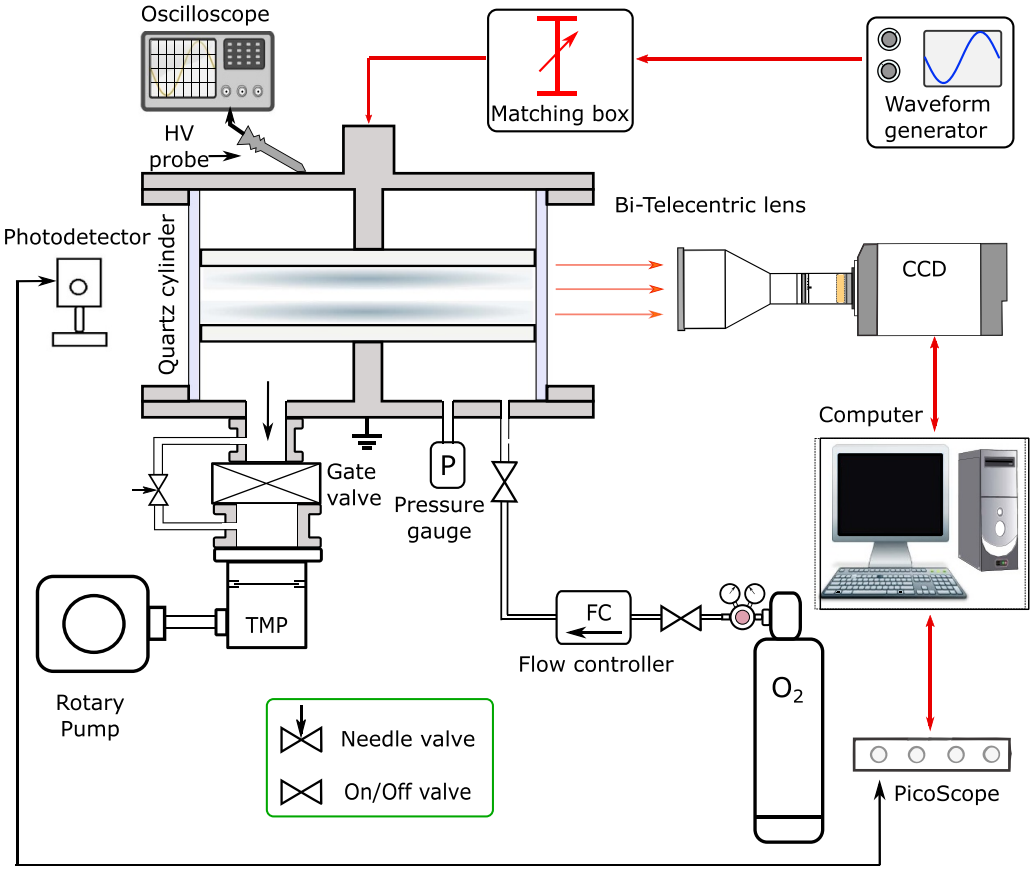


Figure 1. Scheme of the experimental setup.

Table 1. List of collision processes for oxygen CCPs.

#	Reaction	Process	References
1	$e^- + O_2 \longrightarrow O_2 + e^-$	Elastic scattering	[21]
2	$e^- + O_2(r=0) \longrightarrow e^- + O_2(r>0)$	Rotational excitation (0.02 eV)	[22]
3	$e^- + O_2(v=0) \longrightarrow e^- + O_2(v=1)$	Vibrational excitation (0.19 eV)	[22]
4	$e^- + O_2(v=0) \longrightarrow e^- + O_2(v=2)$	Vibrational excitation (0.38 eV)	[22]
5	$e^- + O_2(v=0) \longrightarrow e^- + O_2(v=3)$	Vibrational excitation (0.57 eV)	[22]
6	$e^- + O_2(v=0) \longrightarrow e^- + O_2(v=4)$	Vibrational excitation (0.75 eV)	[22]
7	$e^- + O_2 \longrightarrow e^- + O_2(a^1\Delta_g)$	Metastable excitation (0.98 eV)	[22]
8	$e^- + O_2 \longrightarrow e^- + O_2(b^1\Sigma_g)$	Metastable excitation (1.63 eV)	[22]
9	$e^- + O_2 \longrightarrow O + O^-$	Dissociative attachment (4.2 eV)	[22]
10	$e^- + O_2 \longrightarrow e^- + O_2$	Excitation (4.5 eV)	[22]
11	$e^- + O_2 \longrightarrow O(^3P) + O(^3P) + e^-$	Dissociation (6.0 eV)	[22]
12	$e^- + O_2 \longrightarrow O(^3P) + O(^1D) + e^-$	Dissociation (8.4 eV)	[22]
13	$e^- + O_2 \longrightarrow O(^1D) + O(^1D) + e^-$	Dissociation (9.97 eV)	[22]
14	$e^- + O_2 \longrightarrow O_2^+ + e^- + e^-$	Ionization (12.06 eV)	[23]
15	$e^- + O_2 \longrightarrow e^- + O + O(3p^3P)$	Dissociative excitation (14.7 eV)	[22]
16	$e^- + O^- \longrightarrow e^- + e^- + O$	Electron impact detachment	[23]
17	$e^- + O_2^+ \longrightarrow O(^3P) + O(^1D)$	Dissociative recombination	[23]
18	$O_2^+ + O_2 \longrightarrow O_2 + O_2^+$	Elastic scattering: charge exchange	[23]
19	$O_2^+ + O_2 \longrightarrow O_2 + O_2^+$	Elastic scattering: isotropic part	[23]
20	$O^- + O_2 \longrightarrow O^- + O_2$	Elastic scattering	[23]
21	$O^- + O_2 \longrightarrow O + O_2 + e^-$	Detachment	[23]
22	$O^- + O_2^+ \longrightarrow O + O_2$	Mutual neutralization	[23]
23	$O^- + O_2(a^1\Delta_g) \longrightarrow O_3 + e^-$	Associative detachment	[24]

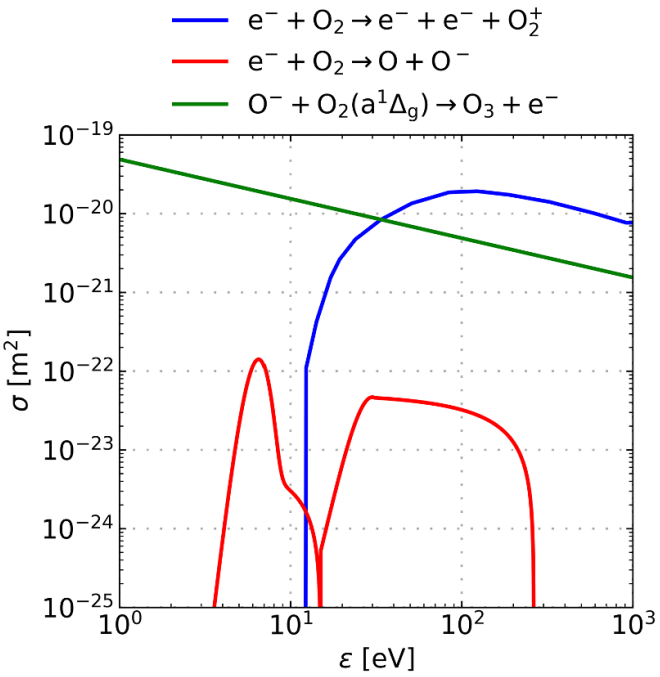


Figure 2. The cross sections of the ionization, dissociative attachment and associative detachment processes.

details in [20]). The $O_2(a^1\Delta_g)$ creation term is the electron-impact metastable excitation rate, which is directly obtained from the simulation, and the loss term corresponds to quenching at the electrodes. Moreover, the $O_2(a^1\Delta_g)$ metastables can also be lost in the associative detachment of O^- ions, however, this channel is negligible in comparison with the surface loss [25]. The cross sections of the ionization, dissociative attachment and associative detachment processes are presented in figure 2, because these processes play an important role in the instability phenomenon studied. Based on previous investigations of the ion composition of the plasma [26–29], although these were carried out at somewhat lower gas pressures, O^- is believed to be the dominant negative ion in the plasma, and the concentrations of O_2^- and O_3^- are significantly lower than that of O^-.

The surface loss rate of $O_2(a^1\Delta_g)$ is governed by the quenching probability, α, which is an input parameter to the simulation. The value of this parameter varies widely for different surface materials [30–33] and has a significant impact on charged particle densities and the electronegativity of the discharge [17, 34, 35]. In this study, an α value of 6×10^{-3} is used, as it has previously shown to yield good agreement between experimental and simulation results for various plasma parameters in studies of oxygen CCPs operated with stainless steel electrodes [17, 20, 25, 36].

The PIC/MCC simulation considers a one-dimensional spatial geometry: the plasma forms between two plane and parallel electrodes separated by a distance $L = 25$ mm. The electrode at $x = 0$ is powered by a single-frequency ($f = 13.56$ MHz) sinusoidal voltage waveform, while the other electrode at $x = L$ is grounded. The driving voltage amplitude, ϕ_0, is varied between 500 V and 700 V, while the gas pressure is kept constant at 100 Pa. The gas temperature is fixed at 350 K. For the elastic reflection of impinging electrons we adopt the probability of $R = 0.7$, based on the findings of [18]. The SEEC, γ, is used as a fitting parameter for finding the best agreement between the experimental and modeling results.

The PIC/MCC code employs an equidistant numerical grid of $N_g = 400$ points with a spatial resolution of $\Delta x = L/(N_g - 1)$ for the calculation of the electric potential and the densities of the charged species. These quantities are computed at discrete values of the time, separated by $\Delta t = T/N_t$ where N_t is the number of time steps within an RF period $T = 1/f$. We use $N_t = 12\,800$ time steps to ensure that the probability of the collisions of the charged species during each time step is kept at a low value. While electrons are advanced at each time step, ions are advanced only in every 20th time step ('ion subcycling'), i.e. $\Delta t_i = 20\Delta t_e$. Following the observation of a significant dependence of the oscillation frequency of the instability on the number of superparticles within the typical range of approximately 10^5, the simulation is implemented on GPU architecture utilizing the CUDA parallel computing platform. This enables the number of superparticles to be increased to approximately 10^6. In this regime, the instability frequency is found to be independent of the number of superparticles. These simulation settings fulfill the stability and accuracy criteria of the PIC/MCC scheme.

The model has been validated experimentally under different discharge conditions resulting in a good agreement between simulation and experiments [17, 20, 25, 36–38].

3. Results

3.1. Experimental results

The instability is identified by the appearance of oscillations in the total light emission from the discharge, as detected by the photodetector. These oscillations appear as a periodic signal in the photodetector output and indicate a periodic modulation of plasma properties. When such oscillations are observed, the corresponding voltage and pressure values are recorded. The detailed experimental conditions and parameters are given below.

The measurements were performed at a fixed frequency of $f = 13.56$ MHz and a gap length of $L = 2.5$ cm, varying the pressure in the range of $p = 50$ Pa to 350 Pa and the voltage amplitude values in the range of $\phi_0 = 250$ V to 700 V.

During the experiments, at each pressure setting, the voltage amplitude was increased until a periodic signal was observed at the output of the photodetector situated in proximity to the discharge cell. The voltage was subsequently increased until the oscillation frequency reached f_{in}, its maximum value. Upon further increasing the voltage, the periodic variation of the light intensity ceased at a specific value of ϕ_0. This procedure was repeated for a series of pressures, and the resulting data are illustrated in figure 3(a). The figure shows the domain where the instability occurs in the pressure-voltage ($p - \phi_0$) plane. No instability was observed below $p < 50$ Pa.

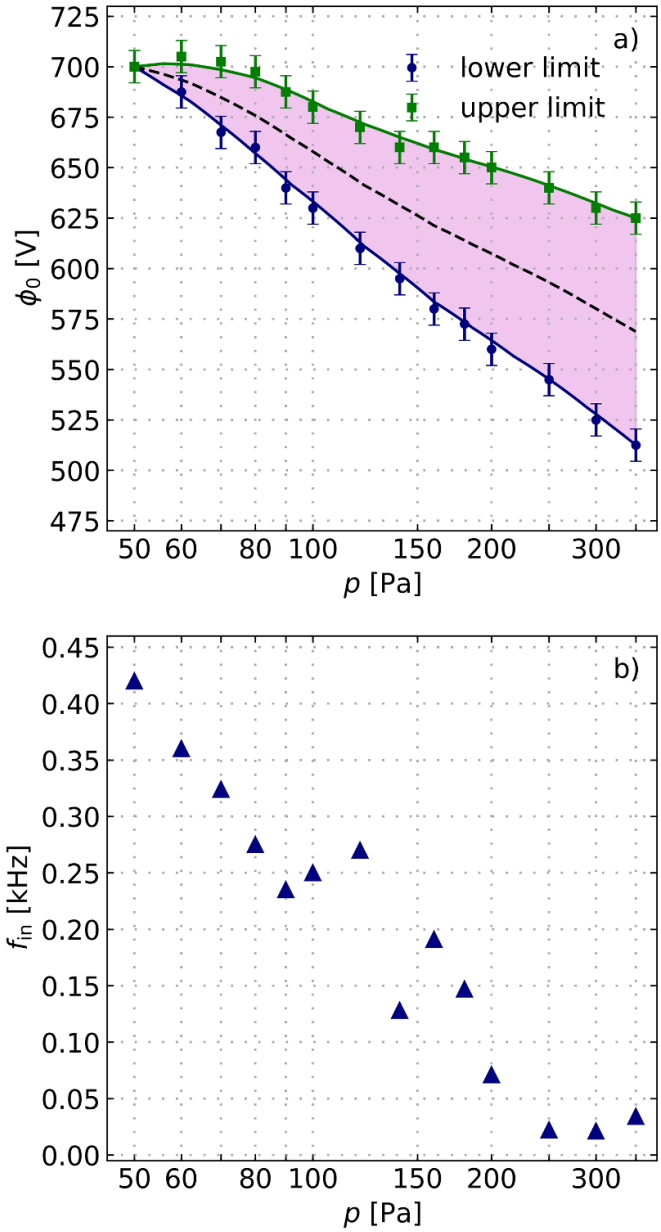


Figure 3. (a) Voltage region of instability and (b) maximum oscillation frequency, f_{in}, as a function of the pressure in the center of the instability region. The dashed line in panel (a) indicates the voltage at which the oscillation frequency is maximum.

The limiting voltages of the instability region were found to be independent of the rate of voltage variation, no hysteresis was observed.

The frequency of the photodetector signal (f_{in}) at ϕ_0, corresponding to the maximum value of the oscillation frequency, is observed to exhibit a strong dependence on the gas pressure, as illustrated in figure 3(b). The frequency decreases with increasing pressure, which can be attributed to the rise in electron density as the pressure is elevated, as will be discussed later.

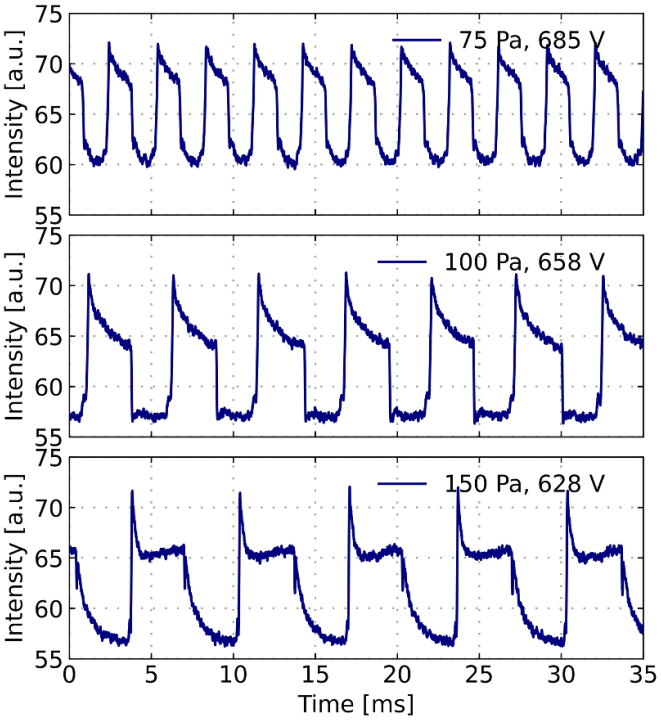


Figure 4. Time evolution of the light emission at different background gas pressures in the center of the instability region as shown in figure 3(a).

Figure 4 depicts the oscillograms at the maximum oscillation frequency for a series of gas pressures. In addition to the frequency variation with the gas pressure, the time evolution of the total light emission exhibits distinct characteristics. Following the rapid low- to high-intensity transition, characterized by a sharp overshoot, the intensity relaxes more rapidly towards a steady plateau level with increasing pressure. However, a similarly sharp intensity variation in the case of high- to low-intensity transitions (falling edge) is only observed at low pressures. For 150 Pa we observe a slow relaxation in the low-intensity domain, with the addition of a small narrow low-intensity peak near the onset of the transition, showing up consistently at higher pressures too.

Figure 5 shows the spatial dependence of the light intensity between the electrodes at a pressure of $p = 100$ Pa for voltages within the range of $\phi_0 = 250$ V to 700 V. Note that the $\phi_0 = 600$ V case is located below the instability region, while the case of $\phi_0 = 700$ V is above it (see figure 3(a)). As illustrated in figure 5(a), the light emission intensity increases monotonically with increasing discharge voltage at every position. For voltages $\phi_0 > 400$ V, an additional maximum emerges in the intensity profile at (or in close proximity to) the electrode surfaces. The position of this peak is independent of both voltage and pressure. The origin of this feature can be attributed to the dissociative excitation of atomic oxygen due to collisions between energetic O_2^+ ions and neutral O_2 molecules, as concluded by Dittmann *et al* [39].

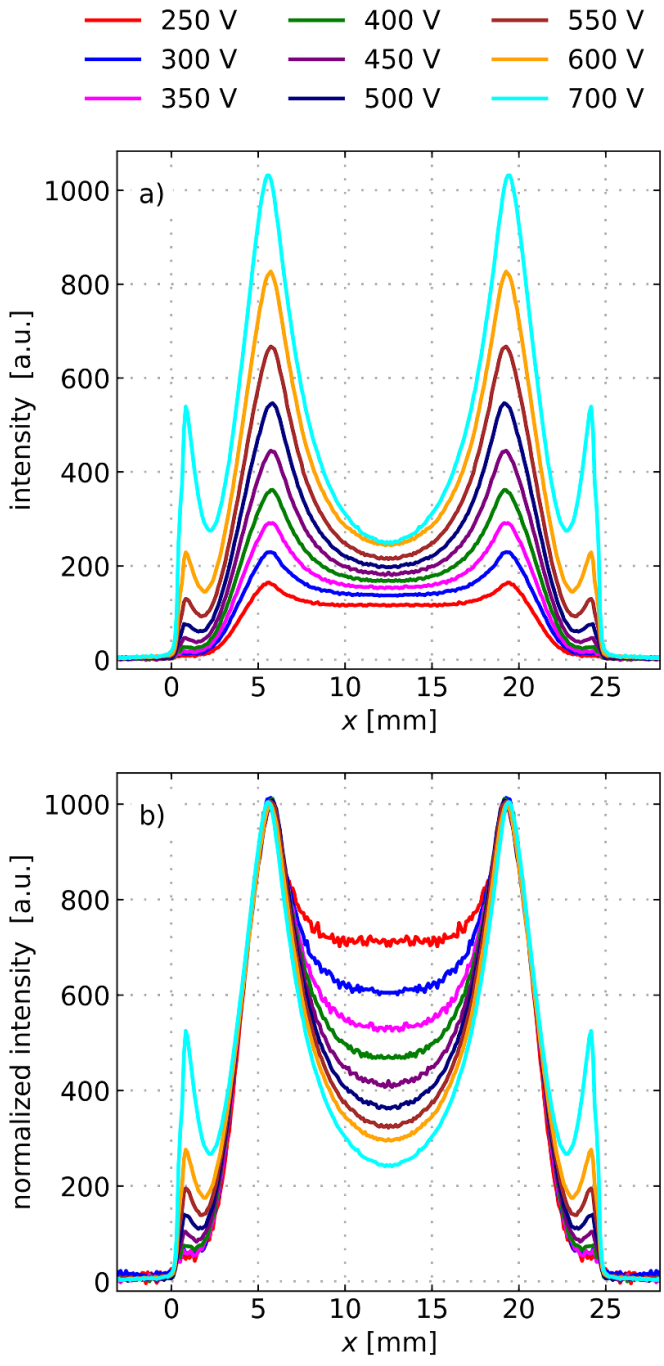


Figure 5. Axial light intensity distributions at $p = 100$ Pa pressure and different voltages. (a) intensities, (b) distributions scaled to have a common peak value.

The data are presented in a normalized form in panel 5(b), with the intensity profiles scaled to have a common peak value. The relative intensities of the various regions (near-electrode peak, main peak, and bulk emission) exhibit disparate variations with increasing voltage. The near-electrode peak shows an increase in relative intensity while the bulk emission displays a decrease in comparison to the main peak intensity. As will be demonstrated later, the overall electronegativity of the discharge decreases with increasing voltage, resulting in a decreased relative contribution of light intensity within the bulk region at higher voltages.

In addition to the stationary axial light emission distributions recorded at conditions outside the instability region, a series of video sequences were recorded at the center of the instability region. The exposure time for each frame was set to 1 ms, which is sufficiently short to allow for the resolution of the different phases of the oscillation. Following the analysis of each frame, the intensity profiles were sorted into two groups, designated as 'high bulk intensity' (HB) and 'low bulk intensity' (LB) modes. As demonstrated in [6], with increasing voltage amplitude the plasma transitions to a 'low electronegativity mode at higher RF power', which is characterized by a reduced bulk electric field and an elevated sheath potential. This aligns with the observed variations in the intensities within the bulk and near the electrodes. Figure 6 illustrates representative examples of instantaneous light emission profiles during the instability. It appears that during the period of instability, the discharge alternates periodically between these two states. At 100 Pa, the HB and LB states differ primarily in the intensities of the bulk and the main peak, which vary in phase. At the higher pressure of 200 Pa, the main peak intensity remains unmodulated; however, the near-electrode peak and the bulk intensities vary considerably but in antiphase.

The observed variations in the spatial distribution of the emitted light during the instability can be understood by considering the following factors. The conductivity of the bulk region increases with decreasing electronegativity, which results in lower bulk emission and smaller potential drop across the bulk region. A smaller potential drop over the bulk results in a larger sheath potential drop at the same applied voltage. The higher sheath voltage accelerates O_2^+ ions to higher energies, peaking at the electrode surface, thereby favoring the excitation of atomic oxygen through the dissociative excitation of O_2 molecules by O_2^+ ions. At higher pressures (200 Pa in this case), the sheath is narrower compared to the 100 Pa case, resulting in an even higher time-averaged sheath electric field. The momentum transfer cross section of O_2^+ ions in O_2 gas decreases with increasing ion energy; therefore, elevated gas pressure does not hinder the ions from gaining higher energies in the higher electric field, which enhances the near-electrode light emission.

3.2. Simulation results

PIC/MCC simulations were conducted at a fixed pressure of $p = 100$ Pa, a frequency of $f = 13.56$ MHz, and a gap length of $L = 2.5$ cm for a series of voltage amplitudes, ϕ_0. The first objective is to match the voltage limits and the oscillation frequency of the instability at this pressure. While all model input parameters are subject to some degree of uncertainty, we have identified the O_2^+ ion induced secondary electron emission yield (γ) as the parameter with the highest degree of uncertainty. Other surface process yields, such as electron reflection (R) and $O_2(a^1\Delta_g)$ metastable quenching (α), have already

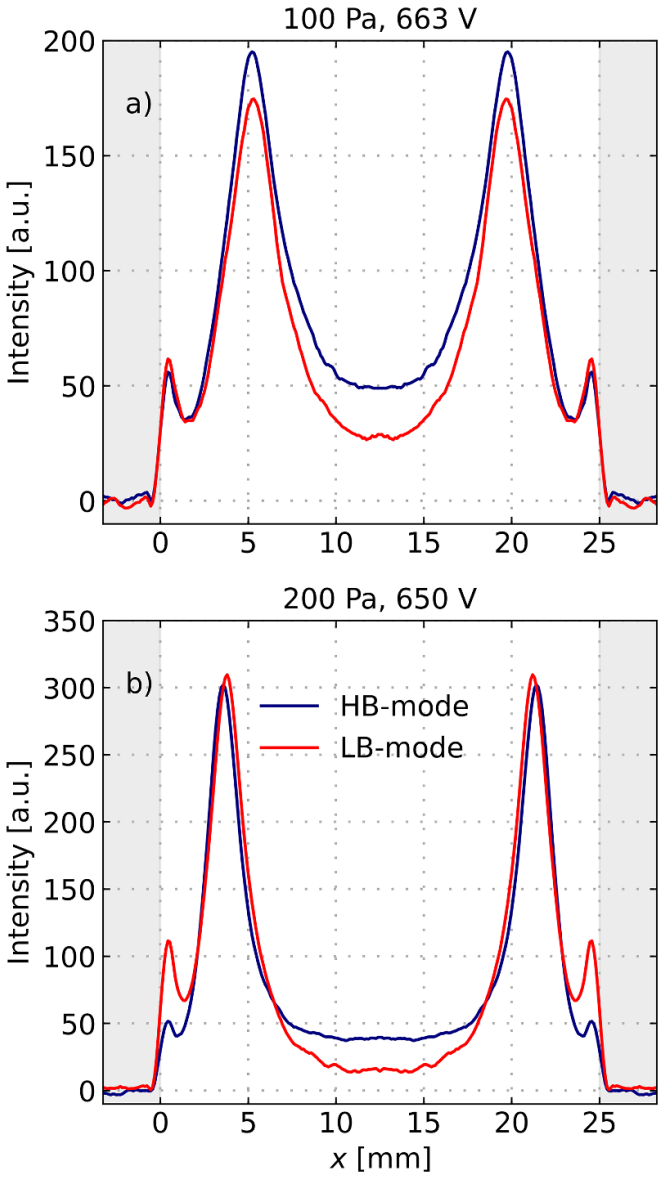


Figure 6. Axial light emission distribution snapshots of oxygen CCPs from the period of instability, at (a) 100 Pa and 663 V, (b) 200 Pa and 650 V. CCD exposure time was set to 1 ms.

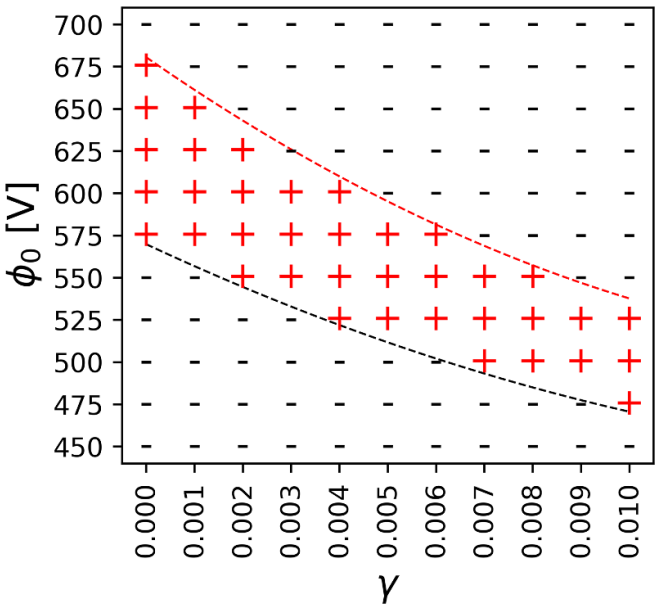


Figure 7. Simulation result of the 'phase diagram' of the instability as a function of voltage amplitude, ϕ_0 and O_2^+ ion induced secondary electron emission coefficient, γ. The black minus and red plus signs indicate the regions of stability and instability, respectively. Discharge conditions: $p = 100$ Pa, $L = 2.5$ cm, $f = 13.56$ MHz, $R = 0.7$, $\alpha = 6 \times 10^{-3}$.

been benchmarked against experimental data [18, 20], and the values that yielded the most consistent results were adopted here and were kept unchanged. In contrast, the γ parameter is treated as a free parameter that has been varied within a physically reasonable range [40].

Figure 7 shows the computed location of the instability region in the γ and ϕ_0 parameter space. The black negative and red positive signs indicate points of stable operation and the presence of instability, respectively. During the simulations, the number of superparticles for each species was recorded after each RF cycle. In cases of stable discharge operation, a smooth convergence of the superparticle number to a stationary value was observed, exhibiting only minimal and uncorrelated statistical fluctuations. At values of (γ, ϕ_0) corresponding to the instability phase, the time evolution of the number of superparticles in the simulation showed very pronounced quasi-periodic oscillations.

As illustrated in the figure, an increase in the secondary electron emission coefficient results in a shift towards lower voltage amplitude in the region of instability. The criteria for instability, as outlined in [7, 8], can be described as twofold: (i) electrons having energies such that the dissociative attachment rate decreases faster than the ionization rate as the electron temperature decreases, and (ii) the negative ion and electron densities are of the same order of magnitude. For a given value of γ, if the voltage amplitude is low, the discharge is highly electronegative, and thus requirement (ii) is not satisfied. However, at sufficiently high voltage amplitudes, the mean energy of electrons increases to a level that prevents the instability from occurring. As the coefficient of secondary electron emission increases, the lower limit of voltage amplitude will decrease, since the additional source of electrons provided by the process will decrease the electronegativity. Similarly, the upper limit of the voltage amplitude will also be smaller, given that secondary electrons acquire high energies as a result of their acceleration by the sheath electric field.

Figure 8 displays the oscillation frequencies within the instability region, which were determined by tracking the temporal variations in the number of superparticles. The frequencies, which fall within the range of $f_{\text{in}} = 0.5$ kHz..3 kHz, are in agreement with the findings of previous simulation and experimental studies [6, 7], as well as the experimental results

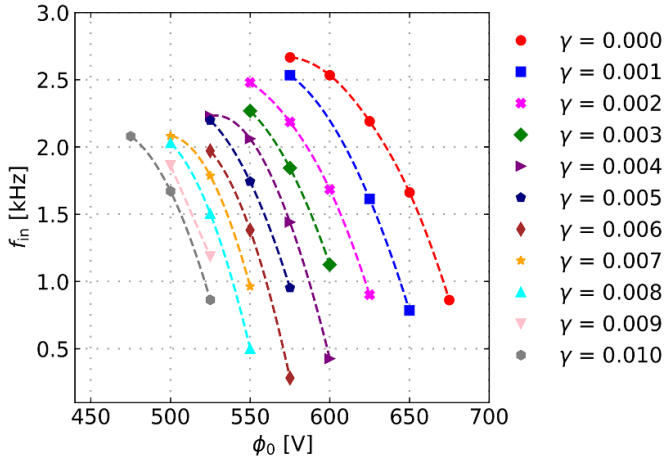


Figure 8. Simulation results of the oscillation frequency, f_{in}, as a function of the voltage amplitude, ϕ_0, for various secondary electron emission coefficient values, γ. Discharge conditions: $p = 100$ Pa, $L = 2.5$ cm, $f = 13.56$ MHz, $R = 0.7$, $\alpha = 6 \times 10^{-3}$.

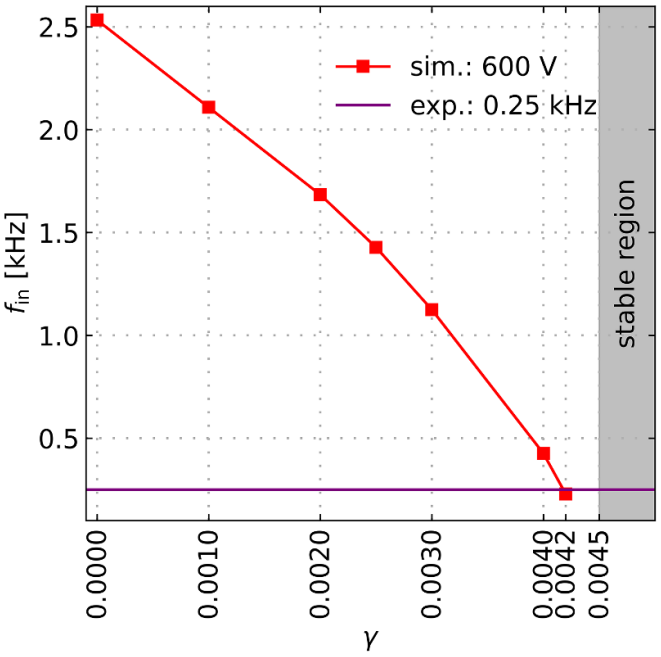


Figure 9. Simulation results of the oscillation frequency, f_{in} as a function of the secondary electron emission coefficient, γ at a fixed voltage amplitude of $\phi_0 = 600$ V. The horizontal purple line presents the experimental value of 0.25 kHz at $p = 100$ Pa, voltage amplitude is $\phi_0 = 655$ V (see figure 3). Discharge conditions: $p = 100$ Pa, $L = 2.5$ cm, $f = 13.56$ MHz, $\phi_0 = 600$ V, $R = 0.7$, $\alpha = 0.006$.

presented above. However, there are slight discrepancies in the specific values observed.

In particular, the oscillation frequency was observed to be $f_{in} = 0.25$ kHz in the case of an applied voltage of $\phi_0 = 655$ V, while the lowest oscillation frequency observed in the simulation was approximately $f_{in} = 0.8$ kHz, as illustrated in the figure. Upon increasing the secondary electron emission coefficient at this voltage amplitude, the instability was no longer observed. To achieve matching frequencies, a reduced voltage amplitude of $\phi_0 = 600$ V was chosen, allowing the experimentally observed oscillation frequency to be reproduced by adjusting the parameter γ. This modification may appear arbitrary at first glance. However, a 10% uncertainty in the voltage measurement is not an unreasonable estimation when considering the potential inaccuracy of the voltage probe and the possibility of a voltage difference between the measurement point (outside the vacuum chamber) and the electrode surface due to electromagnetic effects governing RF power transmission.

This comparison of the experimental and simulation results is presented in figure 9, wherein the experimental value is reproduced at a secondary electron emission coefficient of $\gamma = 0.0042$, which is consistent with the range of secondary electron emission coefficients reported in the literature for comparable conditions [40, 41]. This result indicates that in principle γ can be determined by measuring f_{in} and reproducing it computationally under variation of this surface coefficient, with the assumption that all other model parameters have a reasonably high accuracy.

To gain further insight into the underlying physical processes, simulation results will be presented in the following section using this value of γ and $\phi_0 = 600$ V. Figure 10(a) shows the temporal dependence of the mean species densities (where mean denotes the spatial average over the simulated domain and temporal average over one RF cycle) over multiple periods of the instability. As illustrated in the figure, all charged particle species undergo a gradual decline throughout the instability, followed by a sudden increase. In panel (a), two time instances were selected for further analysis: t_1, which represents an 'intermediate' point in the instability period, and t_2, which is situated in proximity to the aforementioned rapid change in densities. It is noteworthy that the oxygen metastable density exhibits an opposite behavior displaying an initial increase that abruptly declines right after peaking at time t_2. However, this decline is not monotonic. As illustrated in figure 10(b), which depicts the temporal dynamics of the densities in the vicinity of t_2 with enhanced resolution, the oxygen metastable density exhibits two local maxima near t_2.

This behavior can be understood with the aid of figure 11, which shows the mean values of three important reaction rates (S): (i) ionization, (ii) dissociative attachment, and (iii) associative detachment in panel (a), and the corresponding rate coefficients, k (defined as the rates normalized by the mean densities of the collision partners) in panel (b) in the vicinity of t_2. For reference, the electron density and electron temperature are also shown in panel (c) (based on figure 10). The electron temperature is computed from the mean of the particles' kinetic energy $\bar{\varepsilon}$ as $T_e = (2/3)\bar{\varepsilon}$. As the electron density declines gradually until the time instance t_2, the electron temperature rises as shown in panel (c), thereby increasing the rate of dissociative attachment (which has an energy threshold of 4.2 eV) and, among others, the excitation of molecular oxygen leading

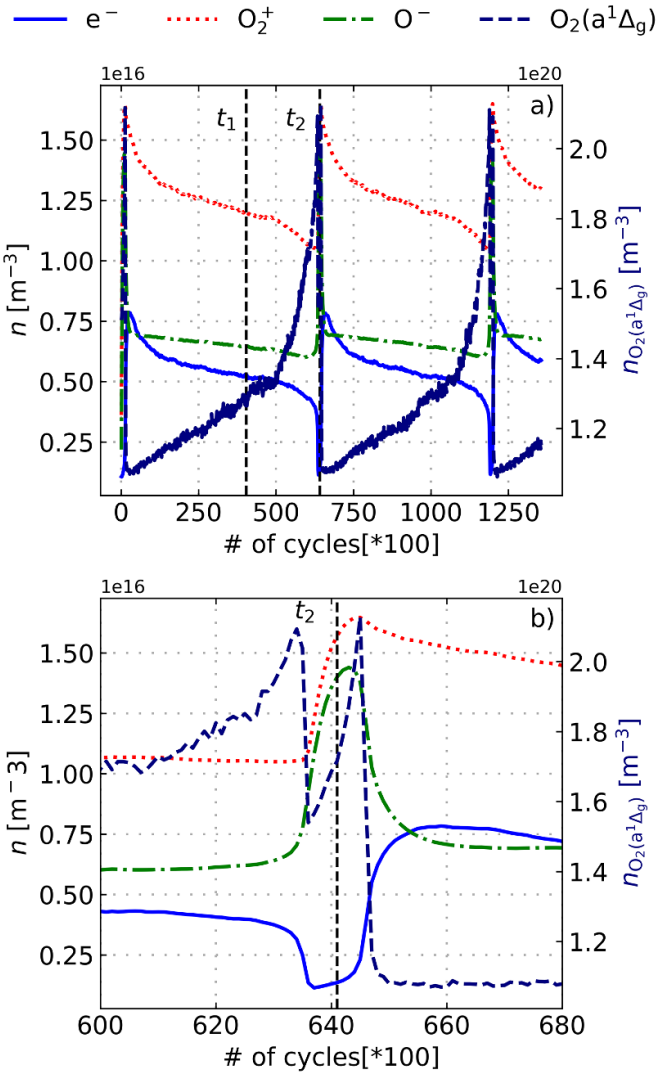


Figure 10. (a) Temporal dependence of mean species densities and (b) their behavior in the vicinity of the rapid increase in charged particle densities. The vertical dashed black lines in the panels indicate moments selected for further analysis. Discharge conditions: $p = 100$ Pa, $\phi_0 = 600$ V, $L = 2.5$ cm, $f = 13.56$ MHz, $\gamma = 0.0042$, $R = 0.7$, $\alpha = 0.006$.

to the generation of oxygen metastables. It is interesting to note that the ionization rate remains nearly constant over this period of time, given that the ionization threshold energy is relatively high, approximately 12 eV. As dissociative attachment represents a loss channel for electrons and a source for negative ions, the electron density decreases at an even faster rate, while the negative ion density and, consequently, the electronegativity of the discharge increase. The high electronegativity enhances the efficiency of ionization within the bulk, thereby increasing the overall rate, as illustrated in panel (a). Concurrently, the elevated mean energy of the electrons gives rise to an enhancement in the dissociative attachment rate, which in turn gives rise to an increase in the negative ion density. This increase will then result in the local minimum in the metastable density, as observed in figure 10(b), due to associative detachment. As illustrated in figure 11(a), following t_2, associative detachment will become the primary electron source. As the electron density increases, the temperature declines, and the metastable density begins to rise once more. The rapid increase of the electron density, resulting from the attachment-induced instability, is illustrated in figure 11(b). Shortly after t_2, a time window emerges where the electron density rises (and, consequently, the electron temperature decreases), yet the rate coefficient of ionization decreases to a smaller extent than that of dissociative attachment. Therefore, despite the decline in temperature, the electron production rate exceeds the loss rate, establishing a positive feedback loop that rapidly enhances the electron density [8].

For a comparison, data obtained at stable operation at somewhat higher voltage amplitude of $\phi_0 = 625$ V (with all other conditions unchanged), are also included in figure 11(as dashed lines). Except for the electron impact creation of O_2^+ ions, the rates in this stable operation case are near the lower bounds of the time-dependent rates observed in the presence of the instability (see figure 11(a)). Similarly, this is also the case for the rate coefficients shown in figure 11(b) and also for the electron temperature displayed in figure 11(c). The only quantity that exhibits an opposite behavior is the electron density, which in the absence of instability is always higher than in the presence of the instability. This is the consequence of the fact that at the higher voltage the discharge operates under lower electronegativity, when there is less creation of negative ions and when the electron temperature is low due to the appreciable electron density in the bulk that results in a high conductivity.

This positive feedback loop is confined to a particular interval of electron energy, and thus the increase in electron density will cease when the electron temperature reaches a sufficiently low level. At this point, all particle densities begin to decline gradually until the electron density falls to a level that permits reinitiation of the feedback loop.

Although this zero-dimensional picture can provide an explanation for the underlying causes of instability, it is of interest to observe the effect of the slow temporal change of the instability on the spatio-temporal dynamics of the plasma. To this end, figure 12 shows the species densities temporally averaged over one RF-cycle for (a) t_1 and (b) t_2. As seen in panel (a), at t_1, when the electron and negative ion densities are comparable, the plasma exhibits an 'electropositive core' [42], with the negative ion density peaking near the edges of the bulk region, while in the center of the discharge, the electron density is maximum. This phenomenon occurs as a result of the creation of negative ions through dissociative attachment from electrons that are accelerated by the electric field in the vicinity of the sheath edges. In the absence of the instability, these negative ions would undergo diffusion towards the bulk, leading to an increase in electronegativity and the formation of a characteristic electronegative core and electropositive edge, as observed in such discharges [43]. This behavior is observed in panel (b) near t_2, where the negative ions are the

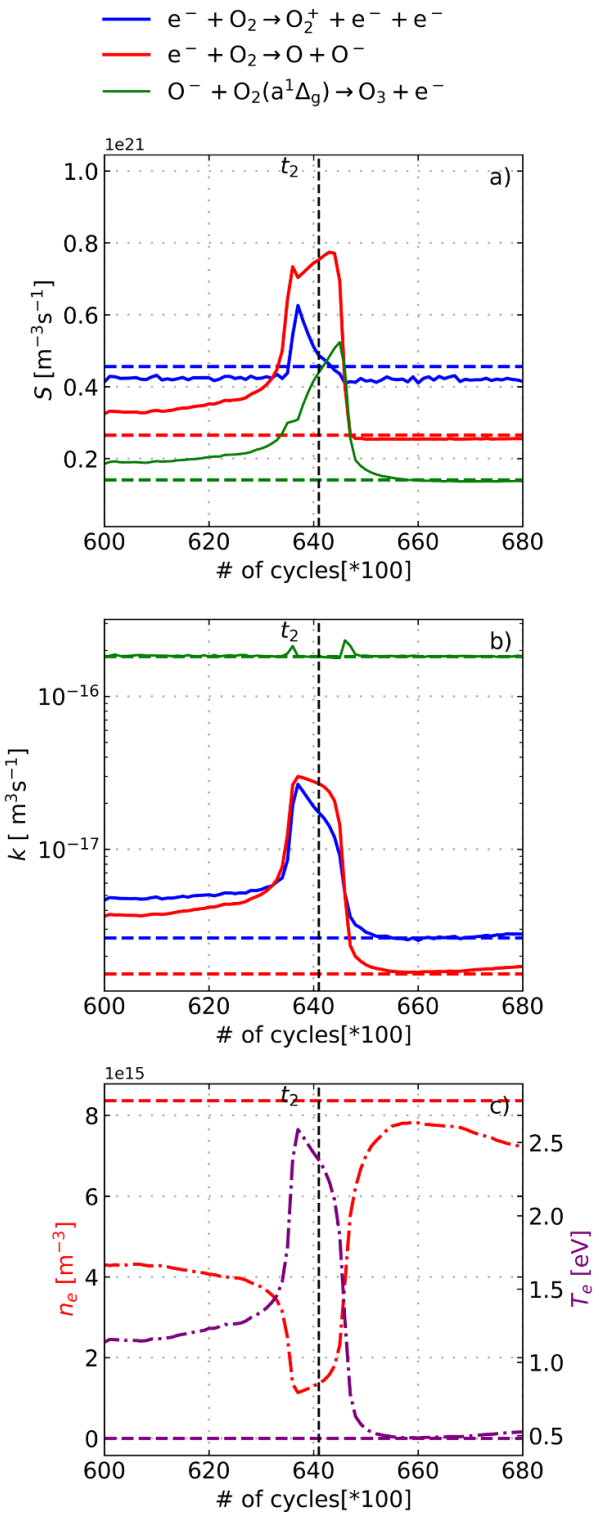


Figure 11. (a) Temporal dependence of the rates S, corresponding to ionization, dissociative attachment, and associative detachment, averaged over space and one RF-cycle near the time instance t_2; (b) the corresponding rate coefficients k, defined as the rates divided by the mean densities of the colliding species; (c) the mean electron density (left axis) and mean electron temperature (right axis), averaged over space and one RF-cycle near the time instance t_2, in units of eV. The horizontal dashed lines in all panels represent the corresponding values of these physical quantities for the case where instability is not observed at $\phi_0 = 625$ V. Other discharge conditions remain the same as in the case of instability except the $\phi_0 = 600$ V. Discharge conditions: $p = 100$ Pa, $L = 2.5$ cm, $f = 13.56$ MHz, $\gamma = 0.0042$, $R = 0.7$, $\alpha = 0.006$.

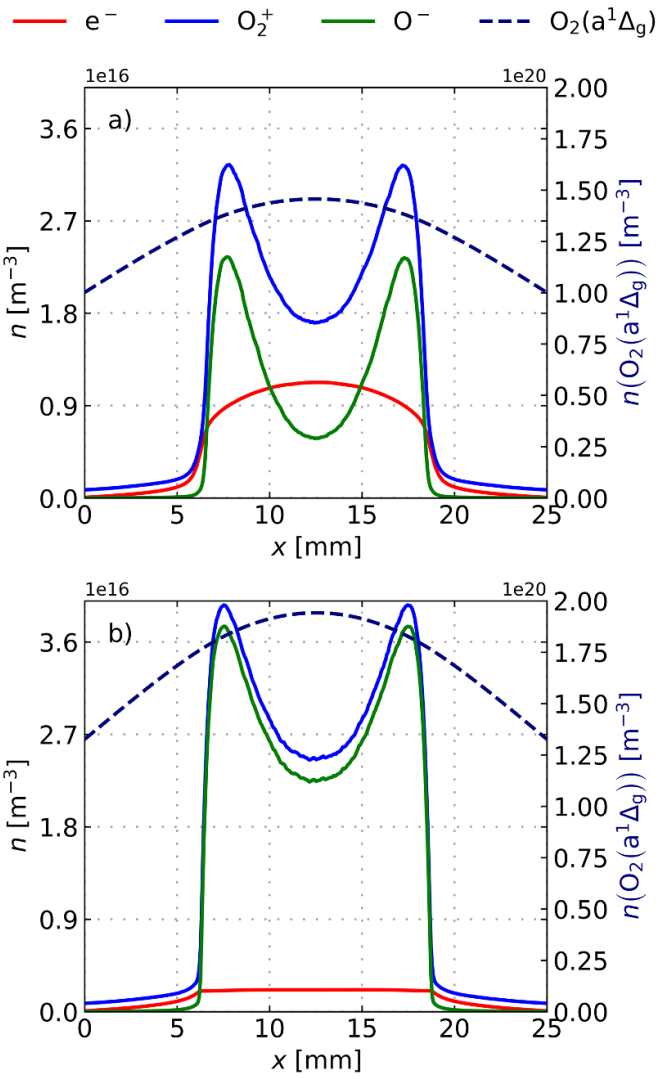


Figure 12. Spatial distribution of the time averaged species densities, n, at (a) t_1 and (b) t_2 as indicated in figure 10. Discharge conditions: $p = 100$ Pa, $\phi_0 = 600$ V, $L = 2.5$ cm, $f = 13.56$ MHz, $\gamma = 0.0042$, $R = 0.7$, $\alpha = 0.006$.

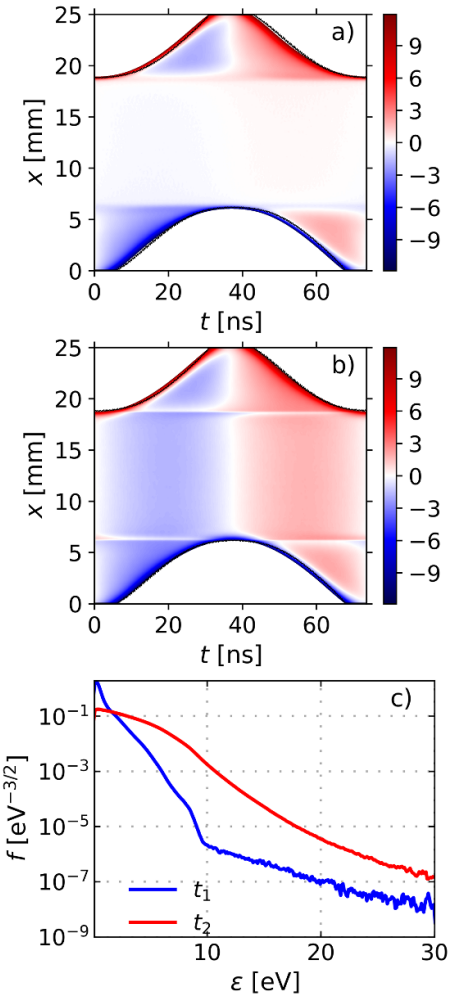


Figure 13. Spatio-temporal distribution of the electric field, E, in the bulk region of the plasma, in units of kV m^{-1}, at (a) t_1 and (b) t_2, as indicated in figure 10, and (c) electron energy probability functions, $f(\varepsilon)$, in the centre of the discharge at t_1 and t_2. Discharge conditions: $p = 100$ Pa, $\phi_0 = 600$ V, $L = 2.5$ cm, $f = 13.56$ MHz, $\gamma = 0.0042$, $R = 0.7$, $\alpha = 0.006$.

dominant negative species in the bulk region. However, due to the instability, the electron density will rapidly increase in the bulk, resulting in the electropositive core observed in panel (a).

As a consequence of the periodic alteration in electronegativity over the timescale of the instability, the discharge will undergo a periodic transition between different power absorption modes. To elucidate this, figure 13 shows the spatio-temporal distribution of the electric field at times (a) t_1 and (b) t_2, as well as (c) the electron energy probability functions, f_{EEPF}, which have been computed in the center of the discharge at these time instances.

In the presence of the electropositive core, the electric field in the bulk is relatively weak, while an electric field reversal occurs near the collapsing sheath to ensure flux conservation. As the electron density decreases, increasing the electronegativity, the characteristic bulk field forms due to the decreased conductivity, as seen in panel (b). This electric field then increases the energy of the electrons, which ultimately leads to the instability described above. This phenomenon is also visible in panel (c), which shows that while at t_1 the EEPF exhibits a depleted high-energy tail and a dominant low-energy region, the increased electronegativity of the discharge and the corresponding bulk electric field accelerate the electrons, resulting in the EEPF acquiring a pronounced high-energy tail allowing an enhanced number of inelastic processes.

The temporal variation of the power absorption mode of the discharge as a consequence of changes in electronegativity is particularly evident when examining figure 14, which shows the spatio-temporal distribution of the three key reaction rates at times t_1 (left column) and t_2 (right column), namely (a, b) ionization, S_{ion}, (c, d) dissociative attachment,

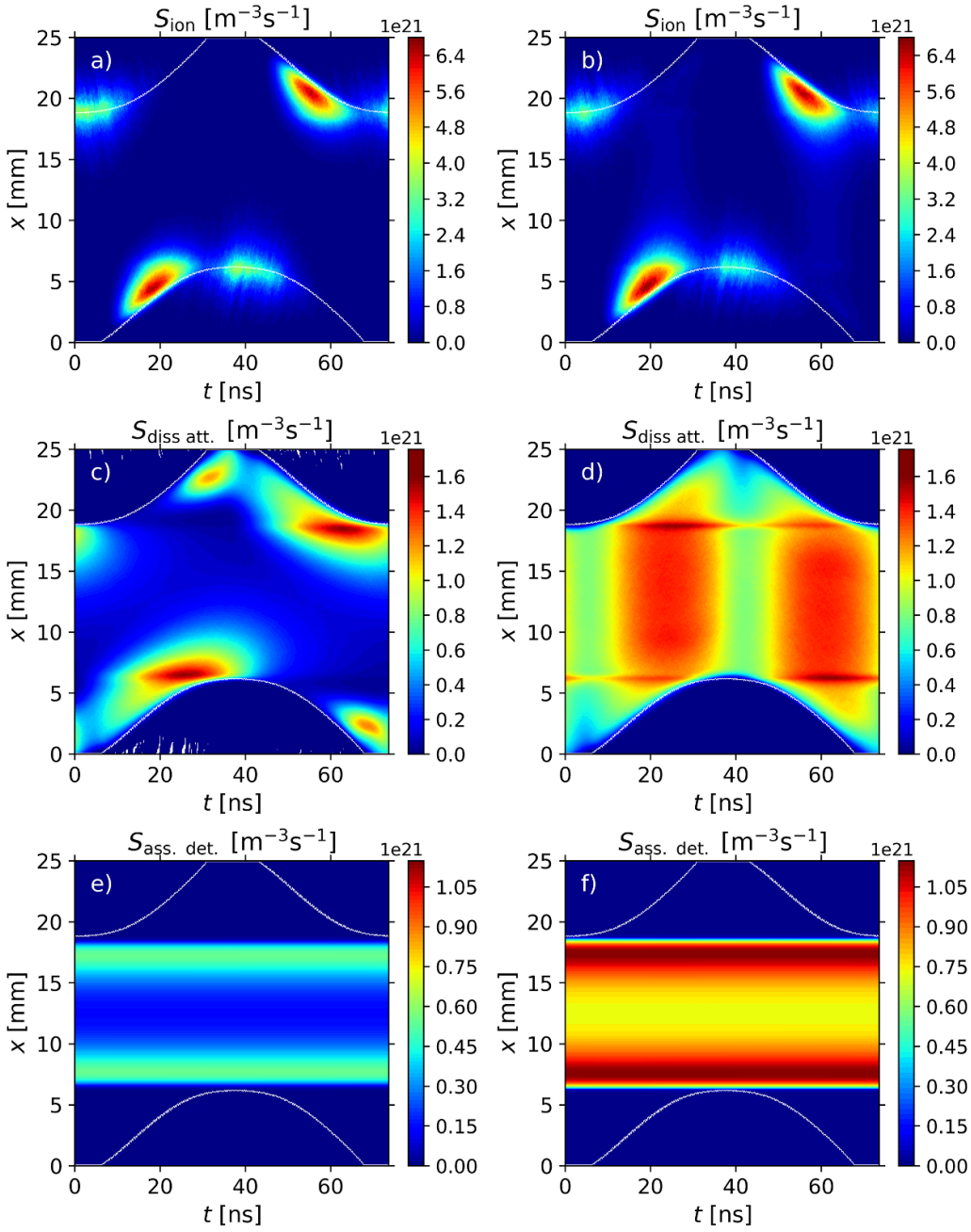


Figure 14. Spatio-temporal distributions of (a), (b) the ionization rate, S_{ion}, (c), (d) dissociative attachment rate, $S_{\text{diss.att.}}$ and (e), (f) associative detachment rate, $S_{\text{ass.det.}}$ at t_1 (left column) and t_2 (right column) as indicated in figure 10. Discharge conditions: $p = 100$ Pa, $\phi_0 = 600$ V, $L = 2.5$ cm, $f = 13.56$ MHz, $\gamma = 0.0042$, $R = 0.7$, $\alpha = 0.006$.

$S_{\text{diss.att.}}$ and (e, f) associative detachment, $S_{\text{ass.det.}}$. The ionization rate at time point t_1 indicates that the discharge is in a detachment-induced (DI) mode [44]. Apart from the α peak, there is a local maximum of the rate near the region of maximum sheath expansion. This can be attributed to the presence of secondary electrons and negative ions created by dissociative attachment near the electrodes, which are then accelerated by the sheath electric field, producing electrons through detachment, and contributing to the ionization peak observed in panels (a) and (d) [44]. Given the weak electric field in the bulk, at this time instance, dissociative attachment is only dominant near the sheath edge, as shown in panel (c). In the interior of the electropositive core, this process is insignificant. The local maxima of the negative ion density near the sheath edges are also the reason why associative detachment (figure 14(e)) is only dominant near the location of maximum sheath expansion, which does not exhibit any temporal variation within one RF-period as negative ions are stationary over this timescale. At time t_2, when the electronegativity of the discharge is increased, the ionization rate is elevated in the bulk

due to the low electron conductivity, which is characteristic of the Drift-Ambipolar (DA) mode [3, 25, 45]. This leads to the increased rate of dissociative attachment in the bulk (panel (d)), which generates negative ions and causes a rise in the associative detachment rate (panel (f)) compared to the situation at t_1. Consequently, the attachment-induced instability gives rise to a periodic alteration in the electron power absorption mode, oscillating between DA and DI modes on a timescale of approximately 500 RF cycles.

4. Conclusion

The phenomenon of plasma instability was investigated in a geometrically symmetric CCP in oxygen. Periodic fluctuations in optical emission intensity were observed under varying conditions of pressure and voltage. To interpret the experimental data, a 1d3v PIC/MCC simulation approach was employed, with a particular focus on the impact of system parameters, including voltage amplitude and the O_2^+ ion induced secondary electron emission coefficient (SEEC, γ), on plasma instability. The γ coefficient was varied at fixed pressure and voltage amplitude in order to achieve the best agreement between the measured and computed oscillation frequencies. This opens a way towards the determination of the γ surface coefficient.

The experimental results demonstrated that the instability occurs within a defined range of voltage amplitudes and pressures exceeding 50 Pa. No instability was observed in the pressure range below 50 Pa. Furthermore, the voltage interval of the instability region exhibited a broadening trend and a gradual decline in its central value with increasing pressure. The oscillation frequency of the emitted light intensity exhibited a pronounced dependence on the gas pressure, displaying a decline with increasing pressure. The spatial distribution of light emission also exhibited variation with voltage, displaying distinctive characteristics in the vicinity of the electrodes, which is associated with the dissociative excitation of atomic oxygen, and within the bulk region.

The experimentally observed oscillation frequency of $f_{\mathrm{in}} = 0.25$ kHz at $\phi_0 = 655$ V was reproduced in the simulation with $\gamma = 0.0042$, at a voltage amplitude of $\phi_0 = 600$ V. It was observed that increasing γ shifted the region of instability towards lower voltage amplitudes, indicating the influence of surface properties on discharge stability. Furthermore, the simulations indicated that plasma instability leads to periodic changes between different electron power absorption modes, characterized by variations in electronegativity and associated shifts in reaction rates, such as ionization, dissociative attachment, and associative detachment.

Data availability statement

The data that support the findings of this study are available upon reasonable request from the authors.

Acknowledgments

This work was supported by the National Office for Research, Development and Innovation (NKFIH) via Grant K134462, by the German Research Foundation via the SFB 1316, project A4, as well as Project 428942393, and by the Grant No. AP19679536 of the Ministry of Science and Higher Education of the Republic of Kazakhstan.

ORCID iDs

Ranna Masheyeva https://orcid.org/0000-0002-6950-662X
Mate Vass https://orcid.org/0000-0001-9865-4982
Murat Myrzaly https://orcid.org/0000-0002-8811-7099
Chong-Biao Tian https://orcid.org/0009-0003-5902-8278
Karlygash Dzhumagulova https://orcid.org/0000-0002-2937-4482
Julian Schulze https://orcid.org/0000-0001-7929-5734
Zoltán Donkó https://orcid.org/0000-0003-1369-6150
Peter Hartmann https://orcid.org/0000-0003-3572-1310

References

[1] Makabe T and Petrovic Z L 2006 *Plasma Electronics: Applications in Microelectronic Device Fabrication* (CRC Press))
[2] Lieberman M A and Lichtenberg A J 2005 *Principles of Plasma Discharges and Materials Processing 2nd edn* (Wiley)
[3] Schulze J, Donkó Z, Schüngel E and Czarnetzki U 2011 *Plasma Sources Sci. Technol.* **20** 045007
[4] Yan M, Bogaerts A, Goedheer W and Gijbels R 2000 *Plasma Sources Sci. Technol.* **9** 583–91
[5] Schüngel E, Mohr S, Iwashita S, Schulze J and Czarnetzki U 2013 *J. Phys. D: Appl. Phys.* **46** 175205
[6] Küllig C, Dittmann K, Wegner T, Sheykin I, Matyash K, Loffhagen D, Schneider R and Meichsner J 2012 *Contrib. Plasma Phys.* **52** 836–46
[7] Descoeudres A, Sansonnens L and Hollenstein C 2003 *Plasma Sources Sci. Technol.* **12** 152
[8] Nighan W L and Wiegand W J 1974 *Phys. Rev.* A **10** 922–45
[9] Katsch H M, Goehlich A, Kawetzki T, Quandt E and Döbele H F 1999 *Appl. Phys. Lett.* **75** 2023–5
[10] Küllig C, Wegner T and Meichsner J 2015 *Phys. Plasmas* **22** 043515
[11] Dong W, Zhang Y F, Dai Z L, Schulze J, Song Y H and Wang Y N 2022 *Plasma Sources Sci. Technol.* **31** 025006
[12] Lieberman M, Lichtenberg A and Marakhtanov A 1999 *Appl. Phys. Lett.* **75** 3617–9
[13] Chabert P, Lichtenberg A, Lieberman M and Marakhtanov A 2001 *Plasma Sources Sci. Technol.* **10** 478
[14] Tuszewski M and White R R 2003 *J. Appl. Phys.* **94** 2858–63
[15] Corr C S, Steen P G and Graham W G 2003 *Plasma Sources Sci. Technol.* **12** 265
[16] Cavarroc M, Jouanny M C, Radouane K, Mikikian M and Boufendi L 2006 *J. Appl. Phys.* **99** 064301
[17] Derzsi A, Bruneau B, Gibson A R, Johnson E, O'Connell D, Gans T, Booth J P and Donkó Z 2017 *Plasma Sources Sci. Technol.* **26** 034002

[18] Schulenberg D A, Korolov I, Donkó Z, Derzsi A and Schulze J 2021 *Plasma Sources Sci. Technol.* **30** 105003
[19] Horváth B, Derzsi A, Schulze J, Korolov I, Hartmann P and Donkó Z 2020 *Plasma Sources Sci. Technol.* **29** 055002
[20] Derzsi A, Lafleur T, Booth J P, Korolov I and Donkó Z 2015 *Plasma Sources Sci. Technol.* **25** 015004
[21] Biagi-v8.9 database Cross sections extracted from PROGRAM MAGBOLTZ, VERSION 8.9 March 2010 (available at: www.lxcat.net) (Retrieved 25 November 2014)
[22] Vahedi V and Surendra M 1995 *Comput. Phys. Commun.* **87** 179–198
[23] Gudmundsson J T, Kawamura E and Lieberman M A 2013 *Plasma Sources Sci. Technol.* **22** 035011
[24] Bronold F, Matyash K, Tskhakaya D, Schneider R and Fehske H 2007 *J. Phys. D: Appl. Phys.* **40** 6583
[25] Horváth B, Donkó Z, Schulze J and Derzsi A 2022 *Plasma Sources Sci. Technol.* **31** 045025
[26] Stoffels E, Stoffels W W, Vender D, Kando M, Kroesen G M W and de Hoog F J 1995 *Phys. Rev.* E **51** 2425–35
[27] Gudmundsson J, Kouznetsov I, Patel K and Lieberman M 2001 *J. Phys. D: Appl. Phys.* **34** 1100–9
[28] Katsch H M, Sturm T, Quandt E and Döbele H F 2000 *Plasma Sources Sci. Technol.* **9** 323
[29] Belostotsky S G, Economou D J, Lopaev D V and Rakhimova T V 2005 *Plasma Sources Sci. Technol.* **14** 532
[30] Greb A, Niemi K, O'Connell D and Gans T 2013 *Appl. Phys. Lett.* **103** 244101
[31] Greb A, Gibson A, Niemi K, O'Connell D and Gans T 2015 *Plasma Sources Sci. Technol.* **24** 044003
[32] Gibson A R and Gans T 2017 *Plasma Sources Sci. Technol.* **26** 115007
[33] Stoffels W W, Kroesen G M W and Schram D C 1993 *J. Phys. D: Appl. Phys.* **26** 1005–12
[34] Godyak V A and Sternberg N 1990 *Phys. Rev.* A **42** 2299–312
[35] Capitelli M, Gorse C and D'Angola A 2001 *Plasma Chem. Plasma Process.* **21** 215–36
[36] You K H, Schulze J, Derzsi A, Donkó Z, Yeom H J, Kim J H, Seong D J and Lee H C 2019 *Phys. Plasmas* **26** 013503
[37] Donkó Z, Derzsi A, Vass M, Schulze J, Schuengel E and Hamaguchi S 2018 *Plasma Sources Sci. Technol.* **27** 104008
[38] Vass M, Wilczek S, Lafleur T, Brinkmann R P, Donkó Z and Schulze J 2020 *Plasma Sources Sci. Technol.* **29** 025019
[39] Dittmann K, Matyash K, Nemschokmichal S, Meichsner J and Schneider R 2010 *Contrib. Plasma Phys.* **50** 942–53
[40] Baragiola R, Alonso E, Ferron J and Oliva-Florio A 1979 *Surf. Sci.* **90** 240–55
[41] Hannesdottir H and Gudmundsson J T 2016 *Plasma Sources Sci. Technol.* **25** 055002
[42] Wang L, Vass M, Donkó Z, Hartmann P, Derzsi A, Song Y H and Schulze J 2022 *Plasma Sources Sci. Technol.* **31** 06LT01
[43] Schulze J, Derzsi A, Dittmann K, Hemke T, Meichsner J and Donkó Z 2011 *Phys. Rev. Lett.* **107** 275001
[44] Tian C B, Wang L, Vass M, Wang X K, Dong W, Song Y H, Wang Y N and Schulze J 2024 *Plasma Sources Sci. Technol.* **33** 075008
[45] Gudmundsson J and Snorrason D 2017 *J. Appl. Phys.* **122** 193302